EUROPEAN ORGANIZATION FOR NUCLEAR RESEARCH

PS DIVISION

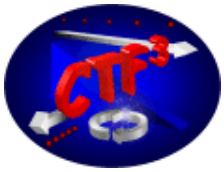

CTF3 Note 018 (MD)
PS/AE Note 2001-011
(Preliminary Phase)

LIL Lattice Parameters, LIL Energy Gains, LIL Temperature versus RF Frequency, EPA Circumference and EPA Isochronicity Measurements

R. Corsini, B. Dupuy, A. Ferrari, L. Rinolfi, T. Risselada, P. Royer, F. Tecker

Abstract

During November and December 2000, MD sessions took place in the LPI complex in order to characterise some specific aspects of the machine before its transformation into CTF3 Preliminary Phase. Following previous studies, some lattice parameters studies and trajectory measurements were carried out in the linac and its model was validated. The calculated and measured energy gains in some of the accelerating sections of the linac were compared with a good agreement. The frequency of the linac was changed around the nominal frequency and temperature compensation proved to be efficient. The EPA ring circumference was measured with the required accuracy for the Preliminary Phase of CTF3. Finally, some isochronicity measurements were performed with the new streak camera and successfully compared to simulations at 308 MeV and 500 MeV.

Geneva, Switzerland
August 27, 2001

1 Introduction

Within the framework of the new CLIC Test Facility (CTF3), some beam studies have been performed in the LEP Pre-Injector (LPI) complex, both on the LEP Injector Linac (LIL) and on the Electron-Positron Accumulator (EPA) ring. The beam studies presented in this note took place in November and December 2000. These sessions of beam studies addressed the following points:

- LIL lattice parameters measurements were made using quadrupole scans and trajectory measurements with various acceleration conditions in order to compare the MAD model of the linac and the machine behaviour.
- Calculated and measured LIL energy gains were checked, and compared to a previous complete measurement campaign made in 1997.
- Controlled variations of the RF frequency and the temperature were tested in the linac. An RF frequency change is needed in both the linac and the RF deflectors will be needed in the CTF3 Preliminary Phase to explore the range of combination factors from 3 to 5 [1].
- The measurement of the EPA circumference was checked with a high precision (about 1 mm) in order to be able to adjust the circumference for a combination factor 4 at the nominal frequency [1].
- Additional measurements with EPA isochronous were performed to get acquainted with the new LEP streak camera and to confirm some previous measurements [2, 3, 4].

In this note, Section 2 deals with the quadrupole scans and the derivation of the Twiss parameters and beam emittance. Section 3 details the trajectory measurement method and its results. Section 4 reports on the LIL energy gains. In Section 5, the experimental tests of the frequency and temperature variations are described and the results are compared to theoretical predictions. Section 6 reports on the measurement of the EPA circumference. Finally, Section 7 deals with the streak camera measurements with both the nominal and the isochronous optics, and compares the results to simulations.

2 LIL Lattice Parameters Measurements

For the CTF3 Preliminary Phase, some modifications of the LPI linac are mandatory: eight of the accelerating structures are removed, a new gun is installed, and a re-arrangement of the remaining components is required. Nevertheless, a valid MAD model of the present linac will be a useful tool for the commissioning of the CTF3 Preliminary Phase. During previous MD sessions [5, 6], some lattice measurements were already performed and compared, with a fair agreement, to simulations made with the TRANSPORT code. However, a new version of MAD with acceleration, which includes the modelling of the RF focusing at the entrance and the exit of the accelerating structures, is now available [7]. In order to improve the accuracy, and to be consistent with the rest of the machine which is described using MAD, the use of this program for the linac is preferable. The aim of this session, which took place in December 2000, was therefore to validate this simulation program against transverse measurements in the linac.

The studied section of the linac was located between the wire beam scanners VL.WBS25 and WL.WBS28 (see Figure 1), where three accelerating sections operate: ACS25-26 powered by the klystron MDK25 and ACS27 powered by the klystron MDK27. The section ACS27 is surrounded by seven quadrupoles. Such kind of arrangement will be used in the CTF3 Preliminary Phase and requires the implementation of dedicated simulation tools in MAD [8].

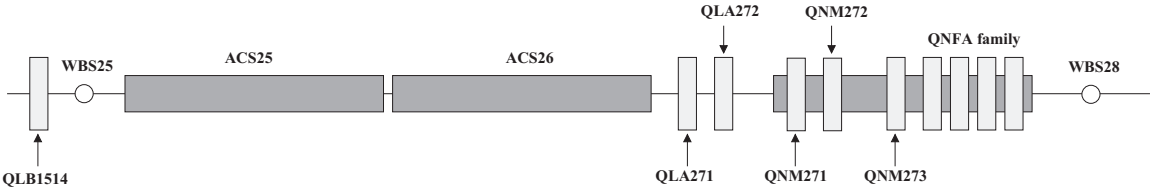

Figure 1: Schematic layout of the LIL section where measurements were performed.

The program was the following:

- Measurement of initial Twiss parameters and emittance with a quadrupole scan in VL.WBS25 using the quadrupole VL.QLB1514 [1)].
- Without acceleration in ACS27, quadrupole scans in WL.WBS28 using quadrupoles WL.QLA271, WL.QLA272, WL.QNM271 (comparison with MAD model, acceleration in ACS25-26).
- With acceleration in ACS27, quadrupole scans in WL.WBS28 using quadrupoles WL.QLA271, WL.QLA272 and WL.QNM273 (comparison with MAD model, acceleration in ACS25-26, acceleration in ACS27 with quadrupoles around the section).

2.1 Initial Twiss parameters and emittance

The initial lattice parameters are found by performing a quadrupole scan in VL.WBS25 using the quadrupole VL.QLB1514, and by deriving the Twiss parameters and the emittance using the usual transfer matrices to describe the linear optics. A single Gaussian model is used to fit the wire scanner beam profiles instead of a double Gaussian model used in the previous reports [5, 6]. The Twiss parameters are consistent between both methods and the emittance is lower in the case of one Gaussian. Indeed, the double Gaussian fit tends to overestimate the importance of the tail of the bunch whereas the single Gaussian better fits the core of the bunch, which is more relevant for the following linear optics treatment.

Figure 2 shows the horizontal and vertical scans in VL.WBS25. The energy $E_0 = 195$ MeV at the entrance of VL.QLB1514 is measured with a good accuracy using the spectrometer magnet VL.BSP15. The transverse parameters at the entrance of the quadrupole are derived from a linear optics fit (emittances are normalised, rms):

- $\epsilon_x = 21\ \pi$ mm.mrad, $\beta_x = 24$ m, $\alpha_x = -0.9$,
- $\epsilon_y = 20\ \pi$ mm.mrad, $\beta_y = 22$ m, $\alpha_y = -0.8$.

These values constitute a reference in the following, and they are used as initial beam conditions at the entrance of VL.QLB1514 in all the simulated scans.

2.2 Quadrupole scans in WL.WBS28 using quadrupoles WL.QLA272, WL.QLA271, WL.QNM271

Initially, the klystron-modulator MDK27 was set to dummy. This is done by delaying the pulse of the modulator compared to the bunch passage so that there is no acceleration in the accelerating sections fed by MDK27. Some energy spectra were monitored at the end of the linac where the beam energy was 150 MeV lower than with the modulator. The aim was first to perform quadrupoles scans in WBS28 without acceleration in ACS27, and then to redo the same scans with acceleration in the section 27. However, the analysis later showed that, by

[1)] VL.QLB1514 stands for the two quadrupoles VL.QLB15.1 and VL.QLB15.4 both powered by the same power supply VL.QLB1514. In the following, the entrance of VL.QLB1514 means the entrance of the first quadrupole of the doublet.

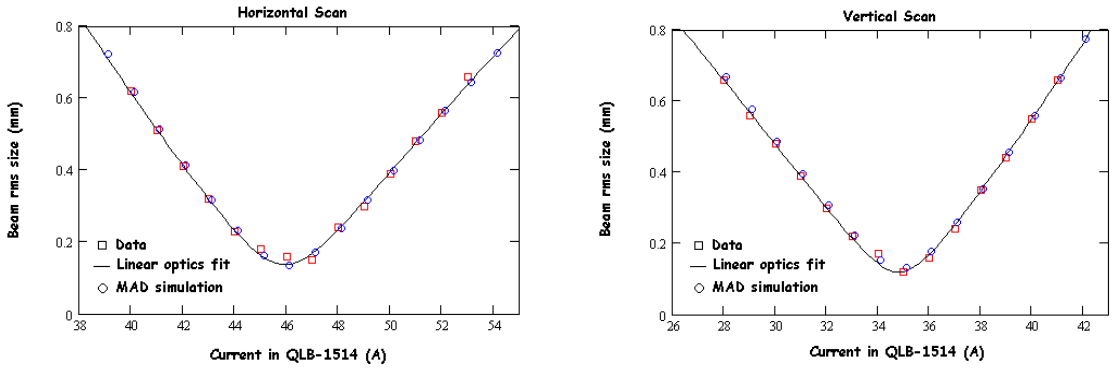

Figure 2: Quadrupole scan in VL.WBS25 using quadrupole VL.QLB1514.

the time the quadrupole scans are performed, the MDK27 was set back to production, either by a wrong manipulation or by a specific modulator timing sent back to the machine through an archive. Figure 3 (left) illustrates this statement in the horizontal plane by showing the data points of the horizontal scans in WL.WBS28 using quadrupole WL.QLA272 with MDK27 on production and supposed on dummy: Data points are exactly the same with and without the modulator MDK27. Figure 3 (right) confirms that simulations are compatible with data when switching on acceleration in the section ACS27. For those simulations, the total energy gain in the acceleration sections ACS25 and ACS26 was set to 102 MeV (see Section 3), and the energy gain in ACS27 was set to 38 MeV.

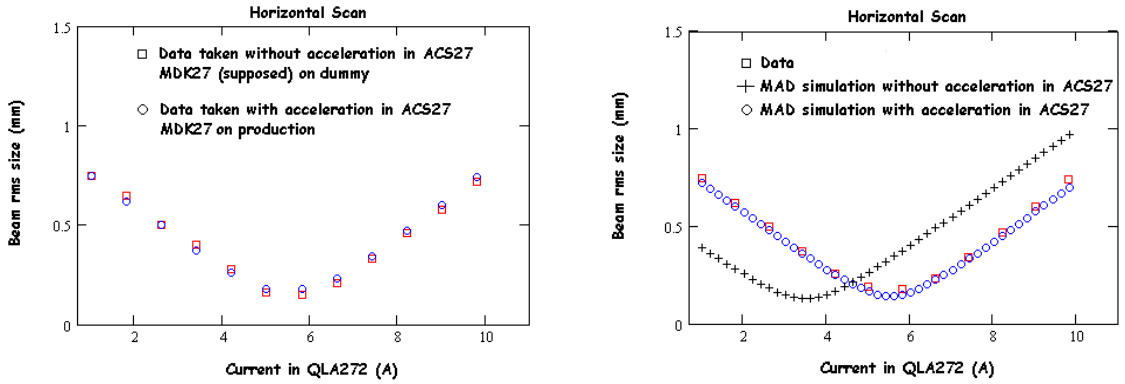

Figure 3: Left: Comparison of data points in the horizontal plane with and without acceleration in ACS27 allows to conclude that MDK27 was on production when it was thought to be on dummy. Right: Experimental (scan with acceleration) and simulated horizontal quadrupole scan in WL.WBS28 using quadrupole WL.QLA272.

In the vertical plane, the scans are performed using the quadrupole WL.QLA271. These scans are less sensitive to the energy variations and the situations with and without acceleration in ACS27 are not clearly distinguishable (see Figure 4). Even though simulations and data are in better agreement in the case of acceleration, a small difference remains between the data and the simulated scan. In the following, this discrepancy is visible on all vertical scans. This is unlikely to be a wrong energy gain since, in the same conditions, the scan using the quadrupole WL.QLA272 (see Figure 3) shows that the energy gain used for the simulations agrees very well with the data. Moreover, small variations on the initial Twiss parameters do not improve the situation. This discrepancy is not yet understood.

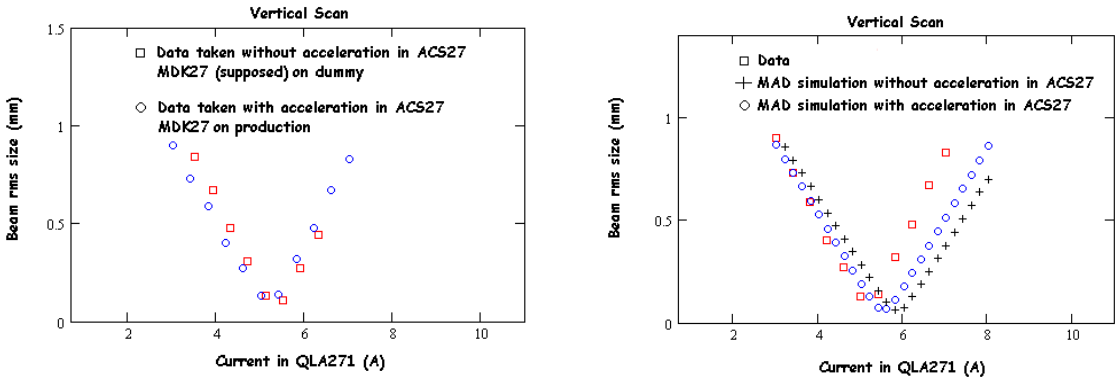

Figure 4: Left: Comparison of data points with and without acceleration in ACS27 allows to conclude that MDK27 was on production when it was thought to be on dummy. Right: Experimental (scan with acceleration) and simulated (same parameters as before) vertical quadrupole scan in WL.WBS28 using quadrupole WL.QLA271.

Another scan was done in WL.WBS28 using the quadrupole WL.QNM271 which is located on the accelerating section ACS27. Since all these scans were performed under the same conditions, the MDK27 was again on production and the simulations with acceleration better match the data points. In this case, however, the vertical plane is more sensitive to energy variations. This sensitivity depends on the behaviour of the betatron functions along the linac and is therefore more important in the horizontal or vertical plane, depending on the quadrupole location. Figure 5 shows the horizontal and vertical scans in WL.WBS28 using quadrupole WL.QNM271 and the simulated scans using the same set of parameters as before.

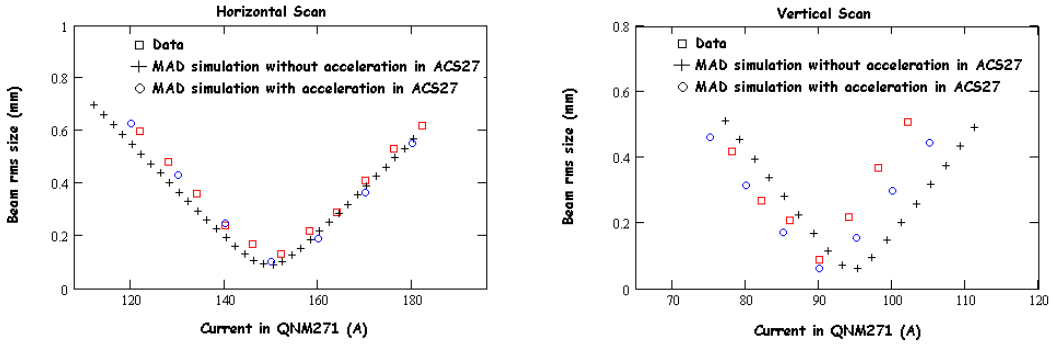

Figure 5: Horizontal and vertical quadrupole scan in WL.WBS28 using quadrupole WL.QNM271. Comparison between MAD simulations with and without acceleration in ACS27.

2.3 Quadrupole scans in WL.WBS28 using quadrupole WL.QNM273

One last scan was done in WL.WBS28 using quadrupole WL.QNM273. It has to be noted that this quadrupole is located on the accelerating section ACS27. Therefore, a new transfer matrix was computed and included in MAD for each point corresponding to each current value. The energy parameters are the same as before. Figure 6 shows that, in the horizontal plane, the simulations match data points very well whereas in the vertical plane, there is always the same discrepancy.

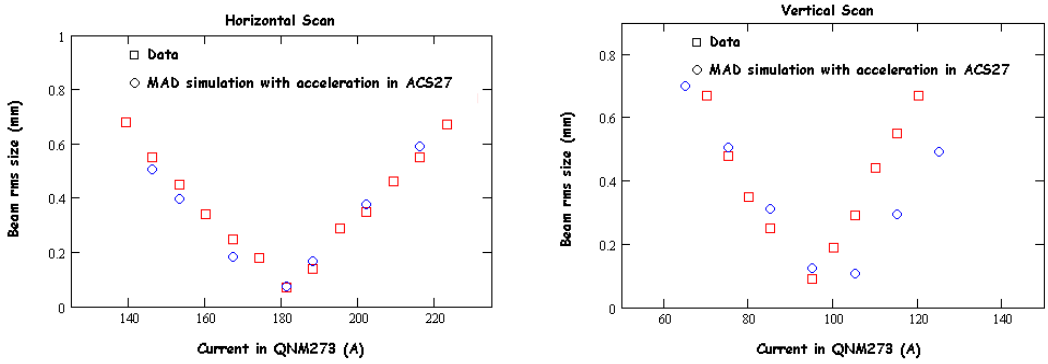

Figure 6: Horizontal and vertical quadrupole scan in WBS28 using quadrupole WL.QNM273.

2.4 Conclusion

The transverse normalised rms emittances found during these measurements (around 20π mm.mrad) were lower than the ones found during the previous sessions (around 40π mm.mrad). As explained before, a single Gaussian fit was used on the wire beam scanner data, instead of the double Gaussian fit as before. This results in a better fit of the core of the bunch on which apply the rules of linear optics.

The energy gains used for the simulations were initially deduced from the values read on the peak power meters. However, the precision was not sufficient and the energy parameters were updated to the correct values after the trajectory measurement analysis (see Section 3). The energy dependence of the scans is therefore critical and a precision below 5% is required on the energy.

The MAD model used to simulate the quadrupole scans with acceleration is in sufficient agreement with the machine. The analytical model of the quadrupoles around the accelerating section [8] is validated against the data. In the horizontal plane, the agreement is very good, whereas in the vertical plane, a discrepancy is visible on all scans. This might result either from a bug in the simulation program, or from a hardware asymmetry between the two planes in the machine. Although not critical, this difference between the two transverse planes will have to be understood in the near future, when more data is available.

3 LIL Trajectory Measurements

A second approach has been used in this MD session to compare the MAD model and the actual machine behaviour. The analysis is based on the trajectory response on single dipole kicks in the beam line.

This method is to some extent complementary to the quadrupole scans previously used. A quadrupole scan provides information about the Twiss parameters and the emittance at a single point. One scan is done to determine the initial conditions at a certain point and a second scan is used at a different location to compare this measurement to the extrapolation by the model of the first scan to this point. The trajectory analysis is independent on the initial Twiss parameters and gives the possibility to compare model and real machine response at each beam position monitor. This opens the possibility to get a view of a larger region of the machine.

A difficulty in the model description of LIL is the increasing energy along the beam path. The MAD model takes into account the energy gain in the accelerating sections, but this energy gain is not well enough known in all parts of the machine to allow a perfect modelling. Therefore, we started our analysis in a limited region of LIL where the energy was constant. Figure 7 shows a schematic view of this region between the beam position monitors UMA27 and UMA31. The beam energy upstream was measured with good precision using the spectrometer magnet VL.BSP15. Then the energy gain in the accelerating sections ACS25 and ACS26 was calculated from the measured RF power at the klystron exit. The modulator MDK27 that feeds ACS27 to ACS30 is set to dummy. This results in the constant beam energy for this region.

The steerers WL.DQL27.1V and WL.DQL27.2H used for this measurement are located on quadrupole magnets just upstream of UMA27. For each of these steerers a reference trajectory was measured and the setting was changed in steps while verifying that the transmission was not affected. The trajectory was measured for each step and the difference to the reference calculated. An example of a difference trajectory is shown in Figure 8. The reproducibility of the measurements was found of the order of $70\,\mu$m RMS.

A first preliminary estimate of the beam energy from power measurements was 298 MeV. The difference trajectory was compared to the model trajectory for this energy. It was then obvious that the betatron phase advance (i.e. the focusing) was lower in the measurement than in the model for both horizontal and vertical plane. This implied that the normalised quadrupole gradients were lower than assumed in the model. Either the magnetic fields were lower or the energy of the beam was higher than expected. Since there are two different magnet types on eight separate power converters in that region we assumed that there was no global error in the excitation constants or current calibrations of the magnets. We also estimated that wake-fields for the low charge used are too small to explain the lower focusing. So we concluded that the beam energy was higher than calculated, probably due to the error of the energy gain calculation.

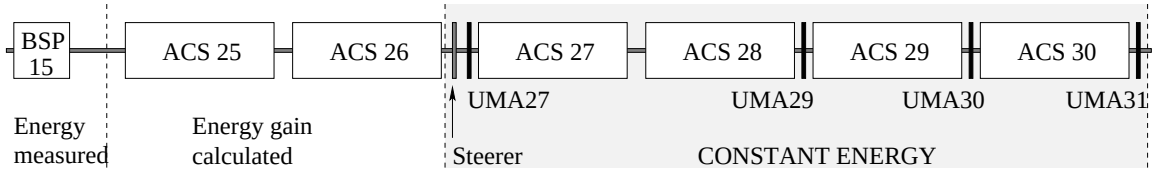

Figure 7: Schematic view of the region used for the analysis, showing accelerating sections and UMAs.

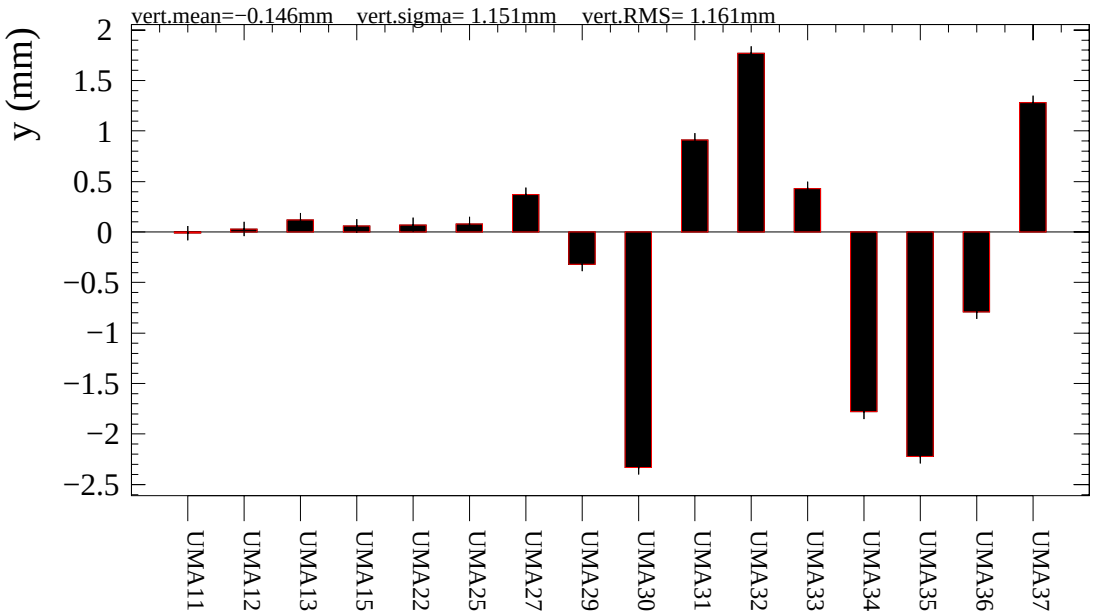

Figure 8: An example of a measured difference trajectory. In this case, WL.DQL27.1V was changed by 6 A.

As a consequence we varied the energy in our model to find the most probable beam energy. At a given energy, the best correction trim strength was fitted to minimise the residual RMS difference between the measured and the model trajectories[2)].

Figure 9 shows the results of measurements taken in November 2000. The minimum residual RMS in the horizontal plane clearly points to an energy of about 308 MeV. This is consistent with the data in the vertical plane indicating 310 MeV as most likely energy. The fact that the energy minimum of a few data sets clearly differs from the rest is assumed to originate from the BPM noise. These data set have the least trajectory change and are thus more affected by the noise. The data sets with the largest current changes indicate that the correspondence between data and model is not perfect since the minimal residual RMS difference is higher than the BPM noise level of $70\,\mu$m. This could be caused by BPM non-linearities or non-linear fields due to the large trajectory change. The analysis of the energy gains (Section 4) shows a beam energy of 311 MeV. This value is consistent with the energy deduced from the trajectory measurements.

The results of a measurement session in December points to the same energy (Figure 10). However, the measured energy in VL.BSP15 is 10 MeV lower than in November, and the energy gain in sections 25 and 26 appears to be identical (same value on the peak power meter). This should result in a 10 MeV lower beam energy, which is not visible on the analysis. On the other hand, the measure of the energy in the spectrometer magnet HI.BSH00 allows to conclude that the total energy gain from MDK25 and MDK31 was 16 MeV higher in December. It is impossible to tell from which MDK this additional energy came from. The precision of this analysis for the energy prediction remains to be checked when more data is available.

[2)] In fact, the measured difference trajectory was corrected using MICADO[9] of the COCU orbit correction package[10], restricting the correction to the one trim that induced the trajectory change. This is equivalent to fitting the trim strength. This method was used because the present version of MAD (8.51/05) did not calculate the trajectory in TWISS correctly when LCAVITY elements (to describe the linear acceleration) were present.

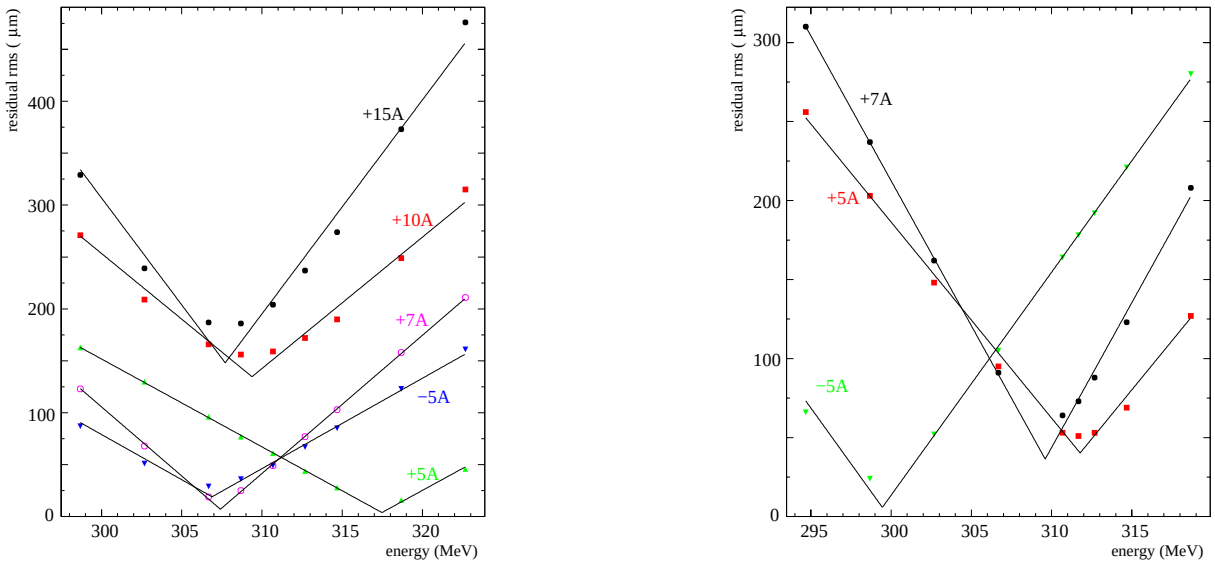

Figure 9: Residual RMS difference for trajectory changes in the horizontal plane by WL.DQL27.2H on the left and in the vertical plane by WL.DQL27.1V on the right. The different data sets were taken for various current changes of the trims. This data was taken on 30.11.2000.

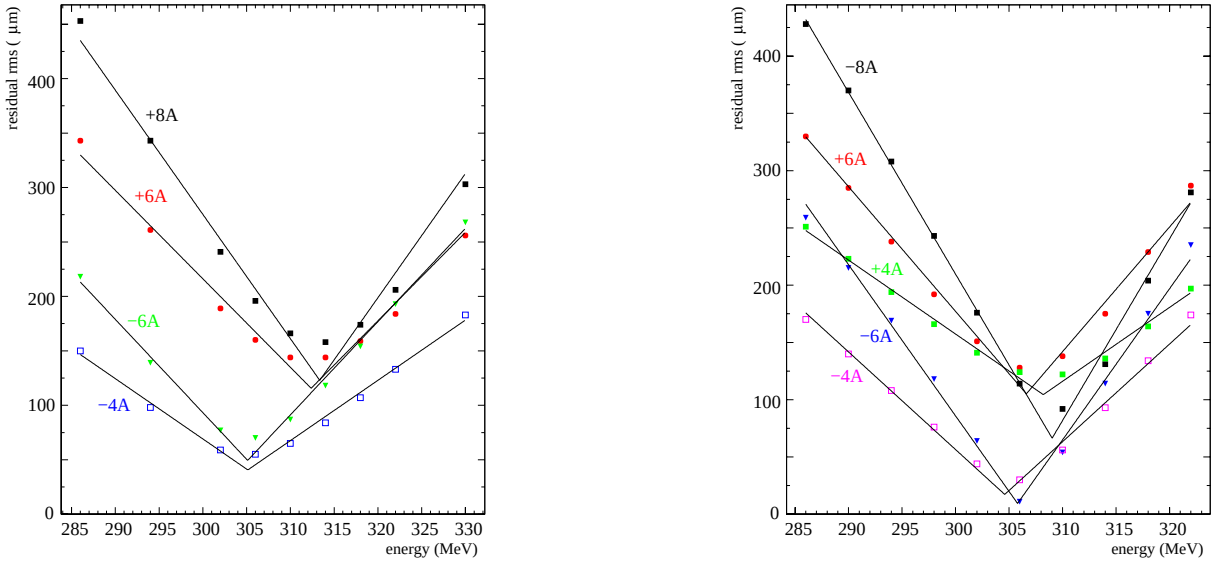

Figure 10: Residual RMS difference for trajectory changes by WL.DQL27.2H on the left and WL.DQL27.1V on the right. This data was taken on 15.12.2000.

In addition to the described measurement, we did take some data for correction coils at different locations in LIL to cover the whole beam path. Some data were taken with MDK27 pulsing so that it is possible to compare the optics in the selected region above with and without acceleration. These data still remain to be analysed.

4 LIL Energy Gains

4.1 LIL Energy Gains Calculations

The calculation of the energy gains in the different accelerating structures in LIL is based on the following formula

$$\Delta E_k = \sum_{i=1}^{n} \sqrt{R'_s L g 10^{-\alpha_i/10} P_k} \quad (1)$$

where

ΔE_k [MeV]	=	Total energy gain obtained after all ACS fed by the klystron *k*
n	=	Number of ACS connected to the klystron *k* [2 or 4]
R'_s [MΩ/m]	=	Shunt impedance of ACS
L [m]	=	Effective length of one ACS
g	=	LIPS multiplication factor
α_i	=	Attenuation factor of the wave guides between ACS *i* and klystron *k*
P_k [MW]	=	Peak power at the klystron exit before LIPS.

For the LIL accelerating structures (ACS), one has:
R'_s = 54.2 MΩ/m, L = 4.5 m, g = 1 (no LIPS), g = 2.27 (with LIPS ON).

An average value for α_i is calculated for each klystron:
$< \alpha_{13} >$ = 6.41, $< \alpha_{25} >$ = 3.36, $< \alpha_{27} >$ = 6.39, $< \alpha_{31} >$ = 6.45.

4.2 LIL Energy Gains measured in 1997

A complete campaign of LIL energy gains was done in 1997 [11]. Careful calibrations of the spectrometer and of the peak power meters were done. The power was also calculated from klystron characteristics and compared with the calibrated peak power meters measurements. Consistent results were obtained between energy gain calculations and beam energy measurements. The results are summarised in Table 1.

	MDK13	MDK25	MDK27	MDK31	Total (MeV)
P (MW)	24.5				
Δ E (MeV)	220				220
P (MW)	24.5	21.7			
Δ E (MeV)	220	99			319
P (MW)	24.5		20.8		
Δ E (MeV)	220		206		426
P (MW)	24.5	21.7	20.8		
Δ E (MeV)	220	99	206		525
P (MW)	24.5			25	
Δ E (MeV)	220			223	443
P (MW)	24.5	21.7		25	
Δ E (MeV)	220	99		223	542

Table 1: LIL energy gains measured in 1997.

4.3 LIL energy gains calculated for the conditions on 29 th November 2000

The following data were recorded with MDK27 OFF. At the beginning, the MDK13 peak power meter indicated 23.5 MW. An energy gain calculated from this value gave 211 MeV. However the measured beam energy provided 206 MeV (2% error). The expected accuracy for the peak power meter readings is not better than 5%. Another source of error could be the LIPS power multiplication factor. If the beam was not passing at the optimised time, g was no more 2.27. In this case, to obtain an agreement with the spectrometer data, the value must be 2.16. The calculated energy gains without MDK27 are reported in Table 2.

	MDK13	MDK25	Total (MeV)
P (MW)	23.5		
Δ E (MeV)	206		206
P (MW)	23.5	24.7	
Δ E (MeV)	206	105	311

Table 2: Calculated and measured LIL Energy gains for MDK 13 and MDK 25.

The energy gain in MDK25 seems to be 102 MeV according to trajectory analysis. This implies a 6% error in the power of MDK25, which is within the accuracy of the peak power meter reading.

4.4 LIL energy gains calculated for the conditions on 15 th December 2000

The following data were recorded during quadrupole scans in WL.WBS28 and LIL trajectory measurements with MDK27 set to OFF. According to the new value of the MDK13 peak power meter (20.4 MW), one calculates an energy gain of 201 MeV. However the measured energy gain was only 196 MeV. This corresponds to the same value of g = 2.16 (or to a 3% calibration error of the peak power meter). According to the quadrupole scans with WL.WBS28 and to the trajectory measurements, the right energy gain for MDK25 was around 102 MeV. The calculated energy gains without MDK27 are reported in Table 3.

	MDK13	MDK25	Total (MeV)
P (MW)	20.4		
Δ E (MeV)	196		196
P (MW)	20.4	24.9	
Δ E (MeV)	196	106	302

Table 3: Calculated and measured LIL Energy gains for MDK 13 and MDK 25.

4.5 Conclusion

The nominal value for MDK13 was always 24.5 MW. The measurements done in November 2000 showed 23.5 MW while those done in December 2000 showed 20.4 MW. This is explained by the change of the PFN value from 35.4 kV to 30 kV, as read on the archives. The power of MDK25 was raised significantly from 1997 but remains almost the same between the two series of measurements. The same remark applies to MDK27 while the power of MDK31 remains always the same. Although important changes in power were done during operation, the calculated energy gains are rather consistent with the measured values and with values derived from beam analysis.

5 Frequency and temperature variation in LIL

The CTF3 bunch train combination scheme requires the condition :

$$C = n\lambda \pm \lambda/N \tag{2}$$

where n is an integer, C is the ring circumference, N is the combination factor and λ is the RF wavelength in the deflectors and the linac. In the CTF3 Preliminary Phase, the range of combination factors from 3 to 5 will be explored by changing the RF frequency of the linac and of the RF deflectors by $\pm$ 150 kHz [1]. The frequency will be changed at the level of the low power RF source. In principle the bandwidth of the klystrons is wide enough to cover this range, with no appreciable changes in gain. The pre-buncher, the buncher, the accelerating structures and the deflectors will be tuned in operation by varying their temperature by $\pm$ 3° C, in order to follow the RF frequency change.

In order to test experimentally this possibility, two series of measurements have been performed on LIL, on November 30 and on December 5. During these tests, in order to be consistent with the CTF3 Preliminary Phase in which no RF pulse compression will be used, the LIPS on MDK13 and MDK31 have been detuned. MDK13 powered the pre-buncher, the buncher and the first four accelerating structures (ACS11 to ACS14) while MDK31 powered four structures (ACS31 to ACS34). MDK25, which has no LIPS, was also used (powering two structures, ACS25 and ACS26).

5.1 Frequency variation

The first series of measurements was done by changing the frequency of the low-level RF source, while keeping the temperature constant at the nominal values (30° C) in all the water stations. As mentioned, the LIPS on MDK13 and MDK31 were detuned far from resonance and the phase-inversion timing was changed to bring it outside the RF pulse duration. The baby klystron source has been disconnected and substituted by a synthesizer. The output power from the klystrons was then checked and no appreciable variation has been observed for a frequency variation from the source of $\pm$ 200 kHz around the nominal frequency.

For beam measurements, the RF frequency was initially set to the nominal value ($f_\circ = 2998.55$ MHz). The bunching system was re-optimised in these conditions and the linac lattice was adapted to the lower accelerating gradient and beam energy by scaling accordingly the quadrupole currents. The steering had to be slightly modified as well, until a reasonable transmission ($\sim$ 70%) was achieved. The beam energy spectrum was then measured in the spectrometers VL.BSP15 and HI.BSH00. Bunch length measurements were also made by the RF phase-energy spectrum method [5], obtaining the value of 6 $\pm$ 1 ps FWHM (see Figure 11-a).

The frequency was then increased to $f_\circ + 100$ kHz and later to $f_\circ + 150$ kHz. In both cases it was possible to recover reasonable beam conditions by re-optimising the bunching system (essentially the buncher phase relative to the first accelerating structure, with minor changes in the other parameters, i.e., amplitude and phase in the pre-buncher and amplitude in the buncher). The transmission was found to be unchanged ($\sim$ 70%) for $f_\circ + 100$ kHz, while it was only $\sim$ 40% for $f_\circ + 150$ kHz. Energy spectra were taken in both spectrometers. The beam energy decreased with respect to the previous value. A bunch length scan was also performed for $f_\circ + 100$ kHz. No appreciable bunch lengthening was found; the results are summarised in Figure 11-b. For a frequency shift higher than $f_\circ + 150$ kHz, it was not possible to recover good beam conditions after the bunching system (beam losses and large energy spread).

At this point, the frequency range below the nominal one was explored. We were unable to find a setting of the bunching system parameters capable of giving reasonable beam conditions for frequencies below $f_\circ - 50$ kHz. At this value, the beam was reasonably well behaved and measurements were still possible. The transmission was $\sim$55%. The beam energy in this case was increased with respect to the initial one. The bunch length scan gave a value of 8 ± 2 ps FWHM, although it must be noted that the measurements are less precise than for the previous cases (see Figure 11-c). The asymmetry of the possible frequency tuning range (without temperature compensation) observed is an indication that, for a temperature of 30° C, the pre-buncher and buncher resonant frequency is about 50 kHz above the nominal operating frequency.

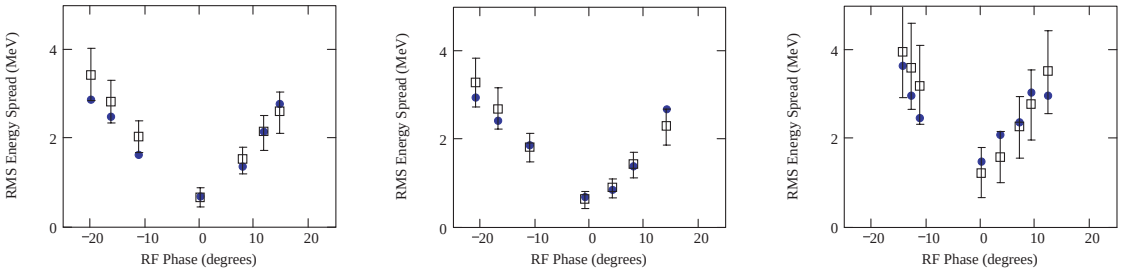

Figure 11: Results of the bunch length measurements with the RF phase-energy spectrum method. The measured rms energy spread is plotted as a function of the RF phase in the accelerating structures (circles) and compared with the calculated values for Gaussian bunches of given FWHM length (squares). From left to right:
Left: Measured energy spread at nominal frequency $f_\circ$, compared with calculated spread for 6 ± 1 ps FWHM bunches;
Center: Measured energy spread at $f_\circ + 100$ kHz, compared with calculated spread for 6 ± 1 ps FWHM bunches;
Right: Measured energy spread at $f_\circ - 50$ kHz, compared with calculated spread for 8 ± 2 ps FWHM bunches.

5.2 Frequency variation with temperature compensation

In the second series of measurements the range $f_\circ \pm 150$ kHz was explored following the frequency variation with a corresponding temperature variation of $\mp$ 3° C around the nominal temperature (30° C). During the beam measurements we monitored also the incident, transmitted and reflected RF signals from the pre-buncher, buncher and accelerating structure, before and after the temperature variation. As expected, the transmitted and reflected signals from the travelling-wave accelerating structures did not show appreciable variations, showing that their bandwidth is large enough to accept the total frequency variation. On the contrary, the pre-buncher and buncher transmitted and reflected signals were affected by the frequency changes, as shown in Figures 12 and 13. Such measurements confirm that the resonant frequency at 30°C in both the pre-buncher and buncher is above the nominal frequency $f_\circ$ by about 50 kHz.

By changing the temperature, it was possible to achieve satisfying beam conditions over the whole frequency range, with constant transmission at about 70%, without adjustments of the bunching system parameters. At $f_\circ - 150$ kHz the temperature compensation was difficult since the interlock system tended to trip the water station no. 2 (pre-buncher and buncher) above 32° C. The compensation appeared to be anyway sufficient. No bunch length scan was

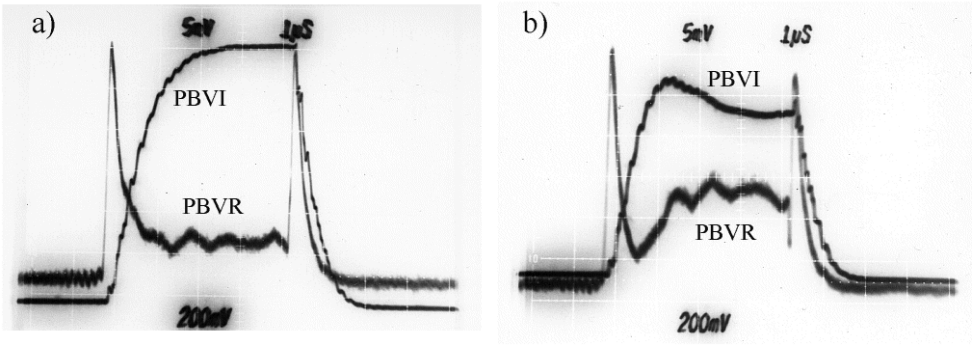

Figure 12: RF signals from the buncher, measured in transmission (PBVI) and reflection (PBVR). Transmitted and reflected signals have different scales (200 mV and 5 mV per division, respectively):
a) For $f_\circ + 150$ kHz, no temperature compensation (30° C). Apart from the normal reflection during the rise and fall of the RF pulse, a small mismatch can be observed in the central part of the reflected signal.
a) For $f_\circ - 150$ kHz, no temperature compensation. The mismatch is now large, as can be seen in both signals.

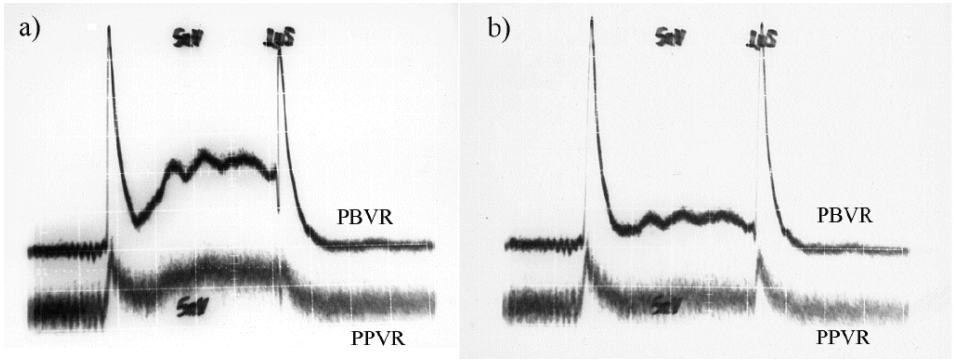

Figure 13: Reflected RF signals from the pre-buncher (PPVR) and buncher (PBVR). The vertical scale is the same (5 mV/division):
a) For $f_\circ - 150$ kHz, no temperature compensation (30°C).
a) For $f_\circ - 150$ kHz, with partial temperature compensation (32° C). A small mismatch is still visible, similar to Figure 12-a.

made, due to lack of time, but the energy spectrum (on-crest) was constant over the whole range and consistent with the typical bunch length of 6 ± 1 ps FWHM. The beam energy with temperature compensation did not change either. In Figure 14 a summary of the beam energy measurements with and without temperature compensation are given. The energy loss is due to dephasing between the beam and the RF field in the travelling wave structures. The expected relative energy loss $\delta E/E$ can be calculated as a function of the frequency variation δf by the (approximated) formula

$$\frac{\delta E}{E} = \frac{1}{\delta\phi} \int_{-\delta\phi/2}^{+\delta\phi/2} \cos\mu \, \mathrm{d}\mu \quad , \quad \delta\phi = 2\pi\tau_{fill}\delta f \tag{3}$$

where τ_{fill} is the structure filling time.

As can be seen from Figure 14, the theoretical evaluation agrees with the measurements, assuming that the synchronous frequency of the structure at the reference temperature is about 80 kHz below the nominal frequency. Such assumption is indeed consistent with previous measurements on the structures [12].

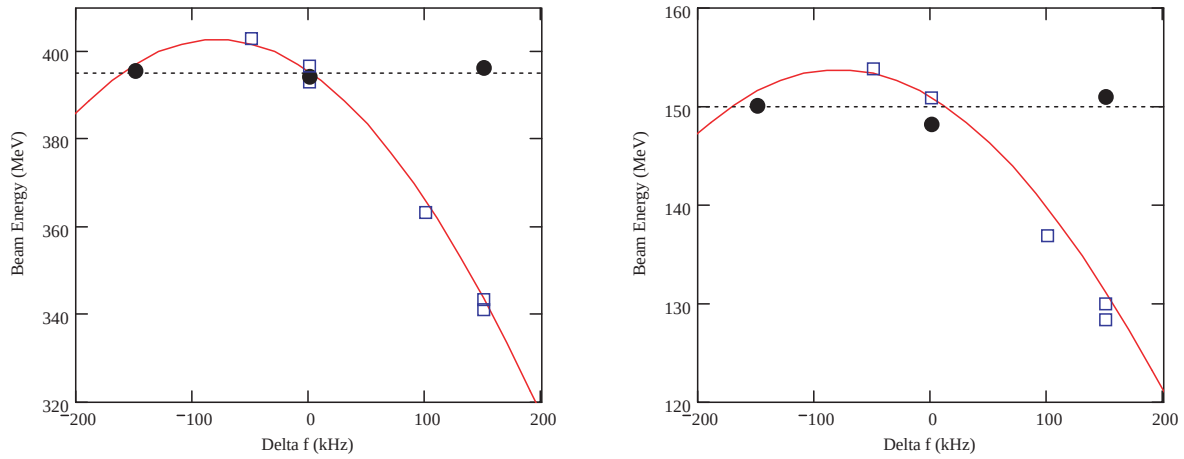

Figure 14: Measurement of beam energy in the spectrometers HI.BSH00 (left) and VL.BSP15 (right), as a function of the frequency variation. The squares are measurements taken at constant temperature (30°C), the circles with temperature compensation. The expected energy variation due to dephasing according to formula (3) is also shown (solid line).

6 Measurements of the EPA circumference

The EPA circumference will have to be adjusted for the CTF3 bunch recombination in 3, 4 and 5 turns. The orbit length will have to be reduced by 17 mm. To prepare this change, the circumference of the present EPA had to be checked with a precision of about 1 mm, *i.e.* a relative precision of 10^{-5}.

6.1 Method

The revolution frequency can easily be changed and measured with such a precision. However, the difficulty is in the control of the *radial position* of the beam, since the circumference has to be measured along the *central* orbit. The average radial position has to be set to zero with a precision better than $1 \text{ mm} \,/\, 2\pi \approx 0.16$ mm. Field errors and orbit correctors are known to modify the relation between beam momentum and orbit length: a kick of 1 mrad at a dispersion of 2 m changes the circumference by 2 mm if the beam momentum is kept constant. For this reason two sets of measurements were carried out: one *with* and one *without* orbit correction. Figure 15 shows that the $\Delta p/p$ differences between the two sets are smaller than $2\ 10^{-5}$.

The momentum error is derived from the closed orbit measurement using

$$\Delta p/p \;=\; \frac{\sum x\ D_x}{\sum D_x^2}$$

where the sums are taken over all position monitors (UMA) in EPA. The choice of this expression for $\Delta p/p$ minimises the rms orbit distortion measured with respect to the ideal orbit positions $\Delta p/p\ D_x$, as may be shown by

$$\frac{d}{d(\Delta p/p)} \sum \left(x - \Delta p/p\ D_x\right)^2 \;=\; 0 \qquad \Longleftrightarrow \qquad \sum \left(x - \Delta p/p\ D_x\right) D_x \;=\; 0 \ .$$

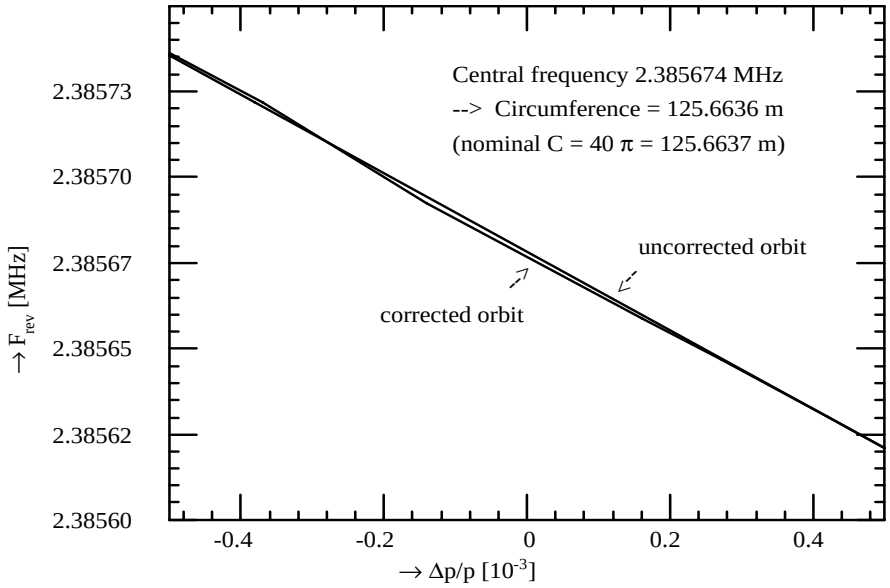

Figure 15: Revolution frequency versus momentum error in the vicinity of the central orbit, measured *before* and *after* orbit correction

The monitors in the long straight sections (where $D_x = 0$) do not contribute to the value of $\Delta p/p$, which is thus insensitive to the orbit distortion in these regions. The quantity $\Delta p/p$ as defined above is therefore more representative for the radial beam position than the simple average $< x >$ over all monitors.

6.2 Results

Figure 15 and Table 4 show that the central momentum corresponds to a revolution frequency of 2.385674 MHz. Taking into account the beam velocity this yields an orbit length of 125.663576 m, *i.e.* only 0.13 mm shorter than the EPA design circumference of $40\pi = 125.663706$ m. This difference is small compared to the required precision of 1 mm.

$\Delta p/p$ $[10^{-3}]$	$< x >$ [mm]	F_{rev} [MHz]
-1.47	-1.22	2.385849
-0.95	-0.79	2.385786
-0.37	-0.32	2.385722
-0.14	-0.13	2.385693
0.16	0.13	2.385659
0.27	0.21	2.385647
0.42	0.31	2.385631
0.69	0.55	2.385600
1.24	1.01	2.385538
1.78	1.40	2.385477

Table 4: Revolution frequency versus momentum error, measured after orbit correction

7 Streak Camera Measurements in EPA with Nominal and Isochronous Optics

Streak camera measurements will be one of the crucial diagnostics for the funnelling experiment during the CTF3 Preliminary Phase. In the present configuration of the LPI complex, some bunch length measurements on the circulating beam can already be performed using a streak camera, to characterise the isochronous optics in the EPA ring. After the recent shut-down of LEP, the LEP streak camera [13] became available and was installed in the EPA synchrotron radiation measurement lab. The aim of this MD session was to get acquainted with the use of this new streak camera and to confirm some previous streak camera measurements [2, 3, 4].
The program was therefore the following:

- Streak camera set-up.
- Micro-bunch profile measurements for the nominal EPA optics at 500 MeV and 308[3)] MeV.
- Micro-bunch profile measurements for the isochronous EPA optics at 500 MeV.

7.1 Streak Camera Set-Up

The LEP camera has 5 different sweep-time scales available as well as a focus mode for which there is no time resolution. Since April 1996, a new tube has been installed in the camera and the manufacturer provided the calibration factors given in Table 5. In the table are also quoted the two fastest factors which have been re-calibrated 2 years later in June 1998 [14]. The sweep times measured in 1998 are 10% to 15% slower than in 1996. A first series of pictures was observed at different time scales to establish the correct operation of the camera, prior to the more systematic study described below.

Range	Sweep time in 1996		Sweep time in 1998	
	ps/mm	ps/pixel	ps/mm	ps/pixel
1000	1054	24.24	-	-
500	264	6.07	-	-
250	155	3.57	-	-
100	104	2.39	120	2.76
50	56	1.29	62	1.43

Table 5: Calibration factors of the sweep time scales of the LEP streak camera (the pixel size of the CCD camera is 23 μm).

7.2 Nominal EPA optics at 500 MeV

The beam is injected axially at 500 MeV and the kicker HR.KFI71 is fired in order to kill the beam on the injection septum after the desired number of turns in the ring. The charge in the pulse is measured with the beam position monitor HIE.UMA22 which counts (taking into account the low gain in UMAs) 154×10^8 particles. The total charge in the pulse is therefore 2.5 nC which is close to the nominal charge for the CTF3 Preliminary Phase where there will be 20 micro-bunches of 0.1 nC each per pulse. Using the SEM-grid HIE.MSH20 at the end of LIL, an energy of 497.8 MeV and an energy spread of 0.55% are monitored.

[3)] The energy of 308 MeV was used for synchrotron light facility in EPA (COLDEX experiment) because the critical energy of photon spectrum at 308 MeV is 45 eV and corresponds exactly to the same critical energy of p^+ in LHC at 7 TeV

Two series of pictures are recorded:

- Using the sweep time scale 1000, for the turns N° 1, 2, 3, 4 and 10.
- Using the sweep time scale 250, for the turns N° 1, 2, 3, 4 and 10.

For each set of measurement, the micro-bunch structure is clearly visible for the first two turns and lost at the third one (see Figure 16). At slower scale, the whole pulse is monitored and up to 20 micro-bunches can be counted (see Figure 16, centre). The correlation seen on these pictures is not clearly understood. The light source is located inside the third bending magnet HR.BHZ56 of the third arc after injection in the ring, where the dispersion is different from zero in the nominal optics. The horizontal beam size is therefore related to the dispersion value at the light source point and to the energy spread. The differences in the horizontal shapes of the bunches over the first three turns could result from a dispersion mismatch at the entrance of the ring. The value of the dispersion at the light source point would then vary from one turn to the other. However, in the nominal optics, this longitudinal mismatch should be small.

Figure 16: Streak camera images for the sweep scale 1000 at first (left), second (centre) and third (right) turns for the nominal optics at 500 MeV.

At faster scale, the micro-bunch profiles are seen with a better resolution. The dependence of the micro-bunch shape on the matching between the injection line and the ring can be seen. Figure 17 shows the bunches after one turn in the ring for two different quadrupole settings in the transfer line. For that time scale, a quantitative study allows the determination of the micro-bunch length and of the micro-bunch spacing.

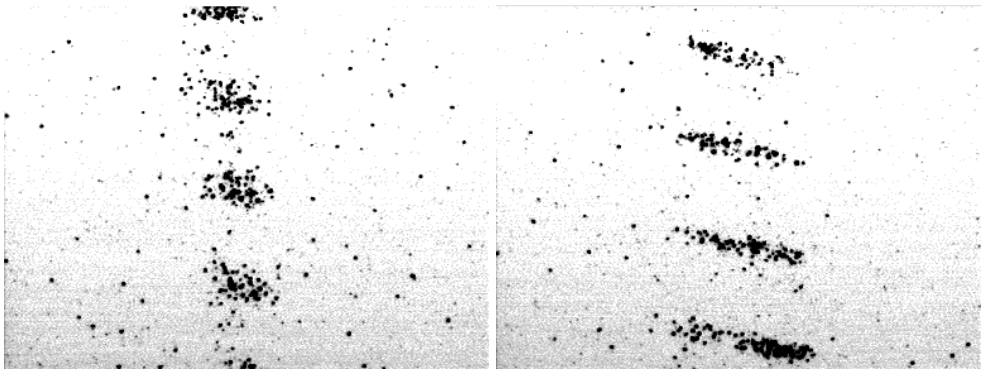

Figure 17: Streak camera images for the sweep scale 250 at first turn for two different quadrupole settings in the transfer line.

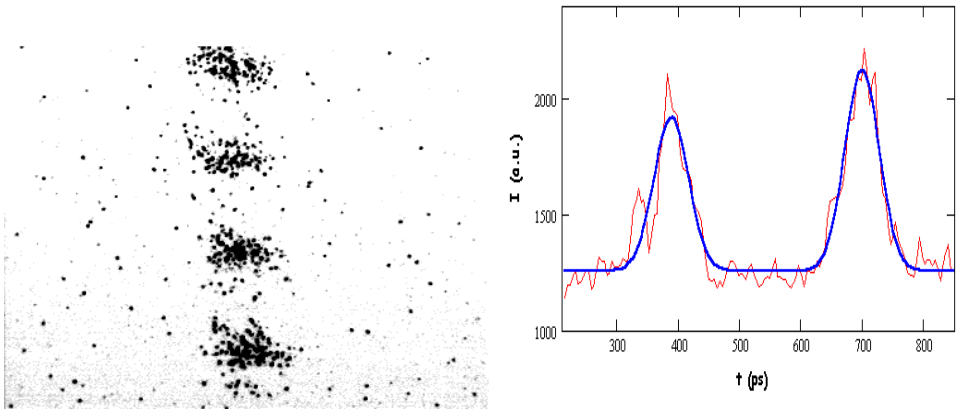

Figure 18: Streak camera image inside the pulse (left) for the sweep scale 250 after the first turn in nominal EPA and the time profile corresponding to the two central micro-bunches (right). The micro-bunch spacing is 311 ps and the micro-bunch length is around 66 ps FWHM.

Figure 18 shows a streak camera image after one turn in EPA, nominal optics at 500 MeV, and the bunch intensity profiles corresponding to the two central micro-bunches. The bunch spacing can be evaluated in the following way: at the end of the linac, the spacing is given by the nominal acceleration frequency of 3 GHz and is therefore 333 ps. However, the beam-loading in the linac results in an energy difference between the micro-bunches at the end of the linac given by

$$\Delta E = P_{bl} \times Q_b = 0.78 \quad \text{MeV} \tag{4}$$

where $Q_b \simeq 0.25$ nC is the charge per micro-bunch estimated to be one tenth of the total charge (although around 20 micro-bunches are visible on the streak camera images, only the micro-bunches located around the center of the bunch are considered the charge is concentrated in the center of the bunch where there are about 10 micro-bunches), and P_{bl} is the beam-loading parameter computed for one bunching cavity and 16 LIL accelerating structures with the values given in [12]

$$P_{bl} = P_{bl,buncher} + 16 \times P_{bl,structure} = 0.056 + 16 \times 0.196 = 3.192 \text{ MeV/nC} \ . \tag{5}$$

After the transfer line and one turn in the ring, the initial spacing is shorter because higher energy particles travel on a longer path length (positive momentum compaction). For the nominal optics , the main contribution to the path length difference is assumed to come from the momentum compaction (or R_{56} factor of the linear transfer matrix R) of both the transfer line and the ring. The small contributions resulting from the dispersion mismatch at the end of the transfer line are neglected. A MAD computation, simulating the optics used during data acquisition of the image of Figure 18, gives $R_{56} \simeq 1.12$ for the injection line and $R_{56} \simeq 4.18$ for the EPA ring between the injection point and the light emission point in HR.BHZ56. The reduction of the bunch spacing is then given by

$$c\Delta T = R_{56}\frac{\Delta p}{p} \tag{6}$$

and corresponds to 27 ps. The expected bunch spacing is therefore around 306 ps. The value of the spacing measured from the fit of Figure 18 depends on the calibration factors read from Table 5. Assuming that the 250 sweep time is now 20% slower than in 1996, the calibration is 4.28 ps/pix. The spacing is then 311 ps, which is close to the expectation.

Using the same calibration, the bunch length of the two micro-bunches, computed from the fit, is 66.8 ps and 66.4 ps FWHM. Equation 6 then allows to evaluate the bunch length at the entrance of the injection line. Using the same values as before for the momentum compaction, an initial bunch length of 7 ps FWHM results in a final bunch length of 61 ps FWHM at the light emission point in EPA, for a Gaussian bunch truncated at $\pm 2\sigma$. Again, the main contribution to the bunch lengthening is the momentum compaction and the other small contributions are neglected. Figure 19 illustrates the bunch stretching between the entrance of the injection line and the light source after one turn in the ring. The value of 7 ps is fully consistent with the bunch length measurements in the linac done during previous MDs [5, 6], where the bunch length was found to be 7 ps FWHM with a precision of ± 1 ps.

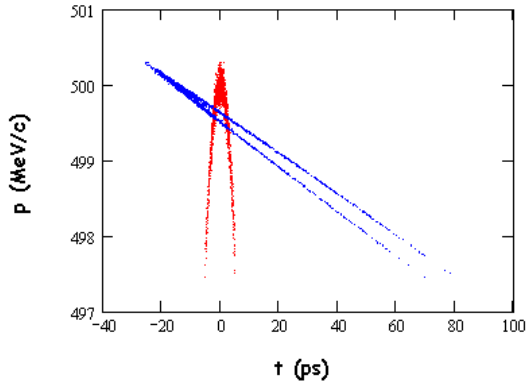

Figure 19: Initial and final truncated Gaussian distributions at the entrance of the injection line and after one turn in EPA, considering the momentum compaction. The bunch lengths are respectively 7 ps and 61 ps FWHM. The shape of the bunch results from the simulation of the RF acceleration in the linac.

In order to evaluate the reliability of the comparison between data and simulation, Table 6 gives the simulated FWHM bunch lengths at the light emission point in EPA after one turn for different initial bunch lengths at the entrance of the transfer line. In spite of the uncertainty on the calibration factor of the streak camera, these values show that the precision on the value of the initial bunch length is high enough. These values are valid if the bunch length is not a by-product of losses during the injection process. The experimental check would be to lengthen the bunch at the entrance of the injection line by accelerating off crest in the linac, and to observe an increased bunch length in the ring, but it was not done during this MD session. Here, we only checked that the energy spread is within the acceptance of the ring ($\pm 1\%$). In addition, during a previous MD session [3], a similar bunch length of 70 ps was found after the first turn in the nominal optics for a higher charge per pulse (3.35 nC) and a higher energy spread (1.7 $\%$).

Initial Bunch Length (ps, FWHM)	Final Bunch Length (ps, FWHM)
6	44
7	61
8	78

Table 6: Simulated FWHM bunch lengths at the light emission point in EPA after one turn for different initial bunch lengths at the entrance of the transfer line. The distribution is Gaussian, truncated at $\pm 2\sigma$.

7.3 Nominal EPA optics at 308 MeV

The next day, with the same conditions of charge and the same injection process, the optics is set for operation at 308 MeV. In HIE.MSH20, the energy spectrum shows an energy of 304 MeV and an energy spread of 0.93%. The aim is to test the light intensity with a different synchrotron light spectrum due to a lower electron energy. From 500 MeV to 308 MeV, the diminution of the integrated light intensity (in the visible spectrum range) is expected to be less than 10% . During the measurements, the micro-bunch structure was visible up to the third turn in the ring and the pictures were similar to what was observed at 500 MeV. As a result, the use of the streak camera is still possible at lower energy, close to the nominal energy for the CTF3 Preliminary Phase, which is 350 MeV.

7.4 Isochronous EPA optics at 500 MeV

With the same conditions of charge per bunch and with the same injection process, the optics is changed to isochronous by modifying the currents in quadrupole families QFL and QTR [15].

Three series of pictures are recorded:

- Using the sweep time scale 250, for the turns N° 1, 10, 20 and 50.
- Using the sweep time scale 250, at turn N° 20, varying the current of the quadrupole family QFL.
- Using the sweep time scale 250, at turn N° 40, varying the current of the sextupole families XNH and XNV.

In such isochronous conditions, the micro-bunch structure is unchanged over a large number of turns: up to 40 turns, the micro-bunch spacing is almost unchanged, as shown on Figure 20. In this machine configuration, the expected bunch spacing is shorter than 333 ps as in the nominal case, but the momentum compaction factor of the transfer line is the only contribution. The computation gives a reduction of 6 ps, and the bunch spacing must be close to 327 ps. However, the transfer line is now badly matched to the ring and some transverse effects may affect this value.

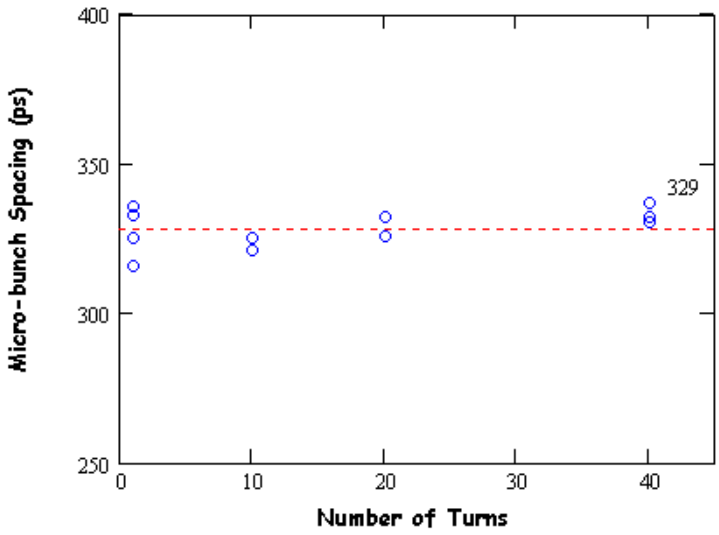

Figure 20: Micro-bunch spacing as a function of the number of turns in the isochronous machine at 500 MeV. The horizontal straight line indicates 329 ps.

Figure 21 shows the micro-bunch time profiles recorded for turns 1, 10 and 20. As written before, the micro-bunch spacing is almost constant, and so is the bunch length measured by curve fitting. For each turn, the mean value of the FWHM bunch length is computed for the three micro-bunches using the same calibration as before and is 33 ps, 47 ps and 47 ps for the 1^{st}, 10^{th} and 20^{th} turn respectively.

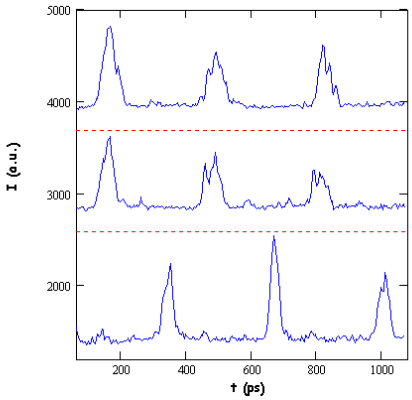

Figure 21: Time profiles of the micro-bunches for turns 1, 10 and 20 (from bottom to top) in the isochronous optics at 500 MeV.

During the second set of measurements, the goal was to check the isochronicity condition by varying the current in the QFL quadrupole family in order to see the transition from a positive to a negative value of the momentum compaction. This is visible through the time-momentum correlation inside the micro-bunches monitored after 20 turns. Figure 22 shows three streak camera images for three different settings of the QFL quadrupole family. The sign of the correlation clearly changes from positive to negative, from left to right. However, in the same time, the micro-bunch shape changes, which shows the importance of the mismatch at the entrance of the ring. This measurement confirms what was observed during previous MD sessions [2].

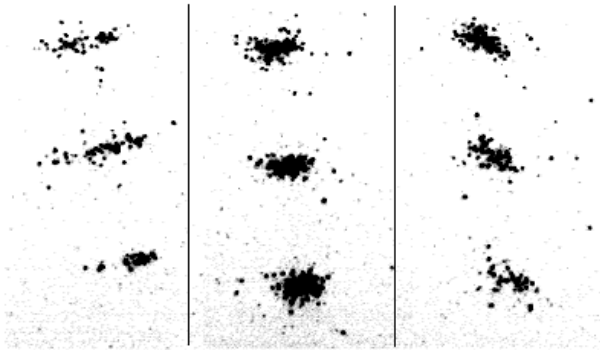

Figure 22: Streak camera images after 20 turns in the isochronous optics at 500 MeV for three different settings of the QFL quadrupole family. From left to right, QFL=88.06, 88.96, 90.06 A. The horizontal axis is energy, the vertical axis is time.

The third set of measurements was dedicated to the observation of the second order of the isochronicity. For that purpose, some pictures are recorded after 40 turns in the machine at 500 MeV with the isochronous optics while modifying the current in the horizontal and vertical sextupole families. Unfortunately, it is hardly possible to see any second order correlation inside the micro-bunches. This measurement should be repeated with longer micro-bunches in order to show the second order inside each micro-bunch.

8 Conclusion

Following the November and December MD sessions, the data analysis presented in this note allowed to conclude on the following points:

- The simulations from the MAD model of the linac are in good agreement with the real behaviour of the machine. In the horizontal plane, the agreement is very good, and in the vertical plane a small discrepancy between data and simulations will have to be understood. The models for acceleration and for the superposition of a quadrupole around an accelerating section are for the time being validated. The quadrupole scan analysis are sensitive to the energy and require a high precision on this parameter.
- The trajectory measurements allow to conclude that the energy gain in the acceleration sections ACS25 and ACS26 is in reasonable agreement with the calculations.
- The comparison between the measured and the calculated energy gains based on peak power meters is rather consistent. However, the expected accuracy of the peak power meter readings (around 5%) should be improved for the Preliminary Phase with a systematic calibration without the LIPS system.
- The study on controlled frequency variation in the linac has shown that the required change of ± 150 kHz around the nominal frequency can be performed when temperature compensation of $\pm 3^{\circ}$C is used, without any effect on the beam parameters. The expected energy variations due to dephasing without temperature compensation is in perfect agreement with the data.
- The study on controlled frequency variation in the linac has also indicated that, for the usual operating temperature, the pre-buncher and the buncher resonant frequency is about 50 kHz above the nominal frequency, while the accelerating structure resonant frequency is about 50 kHz below the nominal frequency. The effects of these discrepancies are small, but an independent setting of the temperature in the two systems will enlarge the accessible range for frequency variation.
- The EPA circumference measurement gives an orbit length of 125.663576 m. This value is only 0.13 mm shorter than the EPA design circumference of 40π. The ring circumference will have to be reduced by 17 mm, corresponding to a frequency in the middle of the range for factor.
- The streak camera which came from LEP after its dismantling is now in operation for the CTF3 Preliminary Phase. The streak camera resolution is practically unchanged when the beam energy is lowered from 500 MeV to 308 MeV.
- The streak camera measurements with the nominal optics gives a bunch length of 66 ps FWHM after one turn in the ring, which is consistent with simulations using an initial bunch length of 7 ps FWHM at the end of the linac. This value confirms previous measurements. With the isochronous optics, the new streak camera images show the micro-bunch spacing unchanged up to 40 turns, and the time-momentum correlation is clearly observable. This also confirms previous observations. Eventually, the recorded images do not allow to see any second order isochronicity effects.

References

[1] R. Corsini, A. Ferrari, L. Rinolfi, T. Risselada, P. Royer, F. Tecker, "Beam Dynamics for the CTF3 Preliminary Phase", CLIC Note 470.

[2] R. Corsini, J.P. Potier, L. Rinolfi, T. Risselada, J.C. Thomi, "First micro-bunch measurements in EPA as isochronous ring at 500 MeV", PS-LP Note 99-03 (BI) (1999).

[3] R. Corsini, L. Rinolfi, T. Risselada, J.C. Thomi, "Report of the 1^{st} June EPA MD", PS-LP Note 99-04 (1999).

[4] R. Corsini, J.P. Potier, L. Rinolfi, T. Risselada, "Isochronous optics and related measurements in EPA", CERN/PS Note 2000-033 (AE) and CLIC Note 440, *Presented at* 7th European Particle Accelerator Conference, Vienna, Austria, 26-30 June 2000.

[5] R. Corsini, A. Ferrari, L. Rinolfi, T. Risselada, P. Royer, F. Tecker, "LIL Bunch Length and Lattice Parameters Measurements in March 2000", PS-LP Note 2000-01 (MD) and CTF3 Note 2000-09 (2000).

[6] R. Corsini, A. Ferrari, L. Rinolfi, T. Risselada, P. Royer, F. Tecker, "New Measurements of the LIL Bunch Length and Lattice Parameters", PS-LP Note 2000-02 (MD) and CTF3 Note 2000-13 (MD-LPI) (2000).

[7] H. Grote, E. Keil, T.O. Raubenheimer, M. Woodley, "Extension of MAD Version 8 to include Acceleration", CERN/SL Note 2000-063 (AP) and SLAC Pub 8491, *Presented at* 7th European Particle Accelerator Conference, Vienna, Austria, 26-30 June 2000.

[8] R. Corsini, P. Royer, "The New MAD Model for the linac of the CTF3 Preliminary Phase", CTF3 Note, in preparation.

[9] B. Autin and Y. Marti, "Closed orbit correction of A.G. machines using a limited number of magnets", CERN ISR MA/73-17 (1973).

[10] W. Herr and J. Miles, "COCU : a closed orbit correction package for SPS and LEP", *Presented in* Workshop on Automated Beam Steering and Shaping (ABS), CERN-99-07 (1999).

[11] LPI Log Book No 10, pages 93 to 122, 17th April to 24th April 1997.

[12] D. Blechschmidt and D.J. Warner, "Parameters of the LEP Injector Linacs", CERN/PS 88-07 (LPI) (1988).

[13] F. Tecker, "Evaluation of the performance of a streak camera in the beam diagnostics at LEP", CERN/SL 95-66 (1995).

[14] A. Burns, private communication.

[15] T. Risselada, "An Isochronous Optics for EPA", PS/LP Note 99-02 (1999).